Properties of electronic potential barriers at grain boundaries in Cu(In,Ga)Se$_2$ thin films

Robert Baier,[1] Caspar Leendertz,[1] Daniel Abou-Ras,[1] Martha Ch. Lux-Steiner,[1] and Sascha Sadewasser[1, 2]

[1)] *Helmholtz-Zentrum Berlin für Materialien und Energie, Hahn-Meitner-Platz 1, 14109 Berlin, Germany*

[2)] *International Iberian Nanotechnology Laboratory, Av. Mestre José Veiga s/n, 4715-330 Braga, Portugal*

(Dated: 11 April 2014)

The lack of an efficiency increase with increasing Ga content in Cu(In,Ga)Se$_2$ solar cells has attracted much scientific interest. It has been claimed that the physical properties of grain boundaries are responsible for this curious effect. Here, we present an in-depth analysis of electronic potential barriers at grain boundaries (GBs) in a series of Cu(In,Ga)Se$_2$ (CIGSe) thin films using Kelvin probe force microscopy (KPFM) measurements, extending our previous study [Sol. Energy Mat. Sol. Cells 103, 86 (2012)]. Here, (i) we show, by comparison with data of the crystal lattice orientations, that localization of GBs purely from KPFM topography data allows reliable localization of GBs. (ii) We consider the averaging effect of KPFM due to long-range electrostatic forces for the analysis of the electronic GB properties to determine the real potential barrier height for each individual GB; we determine potential variations ranging from -400 to $+400$ mV. (iii) We consider the different physical origin of positive and negative potential barriers and present a quantitative analysis of the results to determine charge carrier concentration and defect densities at GBs. From our data and anaylsis we do not observe any systematic variation of these quantities with the Ga content.

I. INTRODUCTION

For many semiconductor materials such as Si[1–3] or GaAs[4–6], it is well known that the presence of grain boundaries (GBs) is detrimental for the electronic material properties. The efficiency of solar cells from these materials is typically reduced by the presence of GBs, due to recombination losses, reduced conductivity, etc. In contrast, solar cells based on polycrystalline $CuIn_{1-x}Ga_xSe_2$ (CIGSe) absorber layers reach excellent power conversion efficiencies above 20%, although a multitudinous number of GBs is present[7]. Therefore, it is generally assumed that GBs either exhibit benign electronic properties, or even support the charge collection process. However, despite intensive research on this phenomenon, the physical fundamentals underlying the electronic properties of GBs in CIGSe thin films remain at the heart of controversial discussions[8–13].

Another curious finding in CIGSe solar cells is that a decrease in efficiency is found when increasing the Ga content to obtain band-gap energies larger than $\sim$1.2eV[14,15]. However, it is expected[16] that the highest efficiencies are obtained for band-gap energies between 1.1 and 1.4eV. It has been claimed, that the properties of the GBs are connected to this efficiency drop for high Ga contents[17,18]. Indeed, significant insight into the GB properties has been gained from Kelvin probe force microscopy (KPFM) experiments, investigating the electronic structure around the GBs[9,10,17,19,20]. While most of the studies have reported a downward band bending at GBs, leading to a transport barrier for the majority carriers (holes in the p-type CIGSe materials), recently also upward band bending has been reported[21–23].

Considering the physics of semiconductors, the potential variations at GBs have been used to quantify charge carrier concentrations and defect densities at GBs[19]. One constraint of such quantifications is the impact of an averaging effect on measured surface potential values, caused by the long-range electrostatic force utilized in the KPFM technique[24]. Due to this, potential variations with a spatial extent on the order of the tip size or below are measured with significantly reduced values. Analytical calculations and numerical simulations have been employed to show that the measured values can be below 20% of the real potential variations, depending on the size of the measured feature, the geometry of the tip, the tip apex radius, and the tip-sample distance[25–30].

Another critical issue in previous studies has been the localization of GBs, which typically has been performed by visual inspection of topography and surface potential images of the

KPFM measurement. Physically correct identification of the GBs requires local diffraction experiments, as obtained by electron backscatter diffraction (EBSD) in an electron microscope. This technique provides the orientation of the crystal lattice of the grains and permits to identify the symmetry of GBs (characterized by Σ values[31]). It was shown that in CIGSe thin films the majority of GBs are high symmetry twin boundaries ($\Sigma3$)[32], which presumably do not show any potential variations[8,20,33]. Thus, a reliable localization of GBs from KPFM measurements would require EBSD measurements of the same sample areas, which is difficult and time consuming, and has been reported only once for a single sample[33].

Here we present a detailed KPFM investigation of the electronic properties of GBs in CIGSe using a series of samples with varying Ga content x. KPFM results on the same samples have revealed up and downward band bending at GBs on the order of ±100 mV[22]. Here we extend this study by additional analyses and conclusions. Initially we demonstrate by comparing EBSD and KPFM data that GB localization from KPFM topography images can be reliably performed by following three simple criteria. Subsequently, the potential variations at GBs are evaluated, finding potential barriers for holes (downward band bending) and for electrons (upward band bending). The different physics of both types of barriers is discussed and the magnitude of the potential barriers is corrected by considering the averaging effect by means of finite element method (FEM) simulations. Finally, values for the charge carrier concentration and defect densities at GBs using the full dimensions of potential barriers are determined.

II. EXPERIMENT

Five CIGSe thin films with [Ga]/([Ga]+[In]) ratios varying from 0 to 1 were grown on Mo-coated soda-lime glass substrates by similar multi-stage co-evaporation processes inside the same evaporation chamber[34]. The growth process leads to a Cu-poor composition of the samples ([Cu]/([Ga]+[In]) < 1). Reference solar cells were processed by chemical bath deposition of a CdS buffer-layer and subsequent sputter deposition of an i-ZnO/ZnO:Al double window layer. Ni/Al grids were used as front contacts. Table I provides an overview of various thin film and solar-cell device parameters of all samples studied in the present work.

KPFM measurements were performed in an ultra-high vacuum (UHV) KPFM setup[35]

TABLE I. Overview of thin film and solar-cell device parameters of the various CIGSe thin films studied.

Sample name	$\frac{[Ga]}{[Ga]+[In]}$	$\frac{[Cu]}{[Ga]+[In]}$	Thickness (μm)	V_{OC} (mV)	J_{SC} (mA/cm^2)	Fill factor (%)	Efficiency (%)
CIGSe-0	0.00	0.82	2.05	490.1$\pm$3.6	36.9$\pm$0.7	72.5$\pm$1.9	13.1$\pm$0.4
CIGSe-33	0.33	0.86	1.72	633.1$\pm$4.2	34.3$\pm$0.5	69.9$\pm$0.5	15.2$\pm$0.3
CIGSe-45	0.45	0.82	2.11	673$\pm$158	28.5$\pm$0.8	74$\pm$20	14.1$\pm$4.9
CIGSe-76	0.76	0.80	2.00	718$\pm$134	13.1$\pm$0.6	51$\pm$6	4.8$\pm$1.0
CIGSe-100	1.00	0.88	1.89	727$\pm$18	13.4$\pm$0.6	55$\pm$3	5.3$\pm$0.4

(base pressure $<10^{-10}$ mbar), using the amplitude modulation technique at the second resonance frequency of the cantilever for detection of the contact potential difference (CPD). The applied ac voltage was 100 mV. For simultaneous topography measurements, the conventional frequency modulation technique at the fundamental cantilever resonance ($f_0 \approx 75$ kHz) was utilized. All measurements were performed using Pt-Ir-coated Si cantilevers at a tip-sample distance of $z \approx 10$ nm. Absolute work function values were obtained from the CPD images by calibration measurements on highly oriented pyrolytic graphite.

Prior to the introduction into the UHV environment of the KPFM, all samples were treated for 2 min in 0.15 M aqueous KCN solution in order to remove surface oxides[22]. To prevent the KCN-treated samples from re-oxidation, they were kept in an environment of deionized water during the transfer into UHV conditions. Directly after introduction into UHV, all samples were annealed at temperatures of about 130°C for 30 min to remove residual water from the surfaces.

The electronic properties of individual GBs were evaluated from KPFM work function images by extracting line profiles perpendicular to the GBs; ten neighboring lines were averaged for the analysis of each GB to reduce the noise level.

Scanning electron microscopy (SEM) and EBSD measurements were performed by use of a LEO GEMINI 1530 SEM, equipped with a field emission gun and a NordlysII-S EBSD detector from Oxford Instruments HKL. The EBSD patterns were acquired and evaluated using the Oxford Instruments HKL software package CHANNEL 5.

Three dimensional (3D) finite element method (FEM) simulations were employed to

simulate the tip-sample interaction in KPFM[28,29]. By minimizing the electrostatic attraction between tip and sample the CPD was calculated. More details about the employed FEM simulations are provided in Ref.[30].

III.   RESULTS

A.   Topography-based localization of grain boundaries

A critical issue in the analysis of the electronic properties of GBs in CIGSe thin films by KPFM is the correct localization of GBs. Previous studies typically consulted both the KPFM topography and work function images to determine the position of GBs[9,10,17,19]. This approach is clearly limited, as GBs with pronounced electronic properties are preferentially selected. A physically correct way to localize GBs is the combination of KPFM and EBSD[33]. In EBSD the positions of GBs are unambiguously determined by an analysis of the crystal lattice orientations of all grains. However, combined KPFM and EBSD experiments are very challenging and time-consuming. Consequently, this method is not suited for extensive studies in which multiple samples are investigated.

For the analysis presented here a different approach was chosen; only topography images are consulted for the determination of the positions of GBs[22]. This approach represents a good compromise between the combination of KPFM and EBSD mentioned above. On one hand, it is not affected by the electronic contrast of GBs in KPFM work function images. Therefore, it promotes the unbiased localization of GBs independent of their electronic properties. On the other hand, it does not require any additional information not accessible by KPFM. Therefore, this approach permits a quick evaluation of the experimental data. The following criteria are applied to localize a GB based on KPFM topography images:

- The GB exhibits a significant change in surface topography with respect to the neighboring grains.

- The shape of the whole grain is perceivable in the topography image.

- If there is any doubt about the origin of a surface feature, it is not considered as GB.

In order to investigate the reliability and the selectivity of this topography-based localization of GBs, this method was compared with GB localization based on EBSD. Fig. 1a

5

shows a KPFM topography image of the CIGSe-0 thin film, in which the locations of all GBs identified according to the above criteria are indicated by numbers ranging from 1 to 25. From the EBSD orientation-distribution map of the identical area (Fig. 1b) GBs can be localized unambiguously based on the crystalline orientation of the various grains of the CIGSe thin film[33]. The identical area of the KPFM measurement was found in the SEM experiment by using markers on the surface. For the following analysis every contact of two grains in the EBSD orientation-distribution map is regarded as a GB. The EBSD pattern-quality map (Fig. 1c) shows GBs as dark lines, where $\Sigma 3$ GBs are highlighted by red solid lines.

In Fig. 2 three representative GBs from Fig. 1 are shown separately; their locations are indicated in Fig. 1a by colored arrows. The non-$\Sigma 3$ GB (Fig. 2a) exhibiting a distinct topography feature is clearly visible in both, the KPFM topography and the Laplace transformed topography images. Fig. 2b shows a highly symmetric $\Sigma 3$ GB with a distinct topography feature, which can be detected in the KPFM topography images. In contrast, the $\Sigma 3$ GB shown in Fig. 2c does not exhibit any topography feature. This GB cannot be noticed in the KPFM topography images. The three GBs depicted in Fig. 2 point out that it is not possible to detect every single GB present in CIGSe thin films based on KPFM topography images. However, Fig. 2 also demonstrates that even highly symmetric $\Sigma 3$ GBs can exhibit
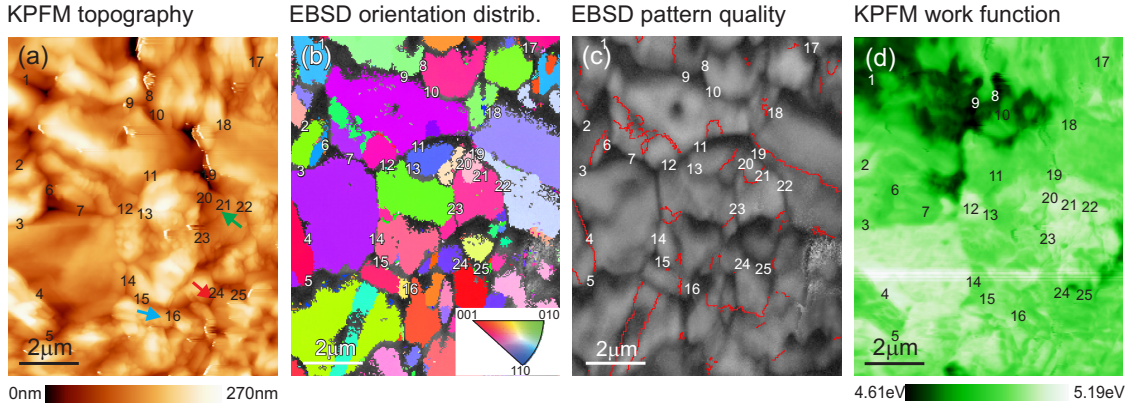

FIG. 1. $9.0\mu m \times 11.3\ \mu m$ (a) KPFM topography image, (b) EBSD orientation-distribution map, (c) EBSD pattern-quality map, and (d) KPFM work function image from an identical area on the CIGSe-0 thin film. In all images the locations of GBs, as determined from the KPFM topography image, are marked by numbers ranging from 1 to 25. In (c) $\Sigma 3$ GBs are highlighted by solid red lines.

6

a change in surface topography sufficient to be localized in corresponding images.

Table II summarizes the results of the analysis by the two GB localization methods. 25 GBs are identified based on the KPFM topography image in Fig. 1a. By comparison to the EBSD measurements of the same area (Fig. 1b and c) they can be classified into two categories: (I) $\Sigma 3$ GBs and (II) non-$\Sigma 3$ GBs. About 10% of the identified GBs are classified as $\Sigma 3$ GBs. All other GBs exhibit non-$\Sigma 3$ symmetries. It is noteworthy that no surface features are misinterpreted erroneously as GBs. For comparison, by EBSD-based localization of GBs 97 GBs are detected within the same surface area. More than 35% of the GBs exhibit a $\Sigma 3$ symmetry, all other GBs reveal a non-$\Sigma 3$ symmetry. The frequency of detected $\Sigma 3$ GBs is lower than reported previously[32] due to shadowing effects resulting from the larger surface roughness of the present samples compared with polished surfaces.

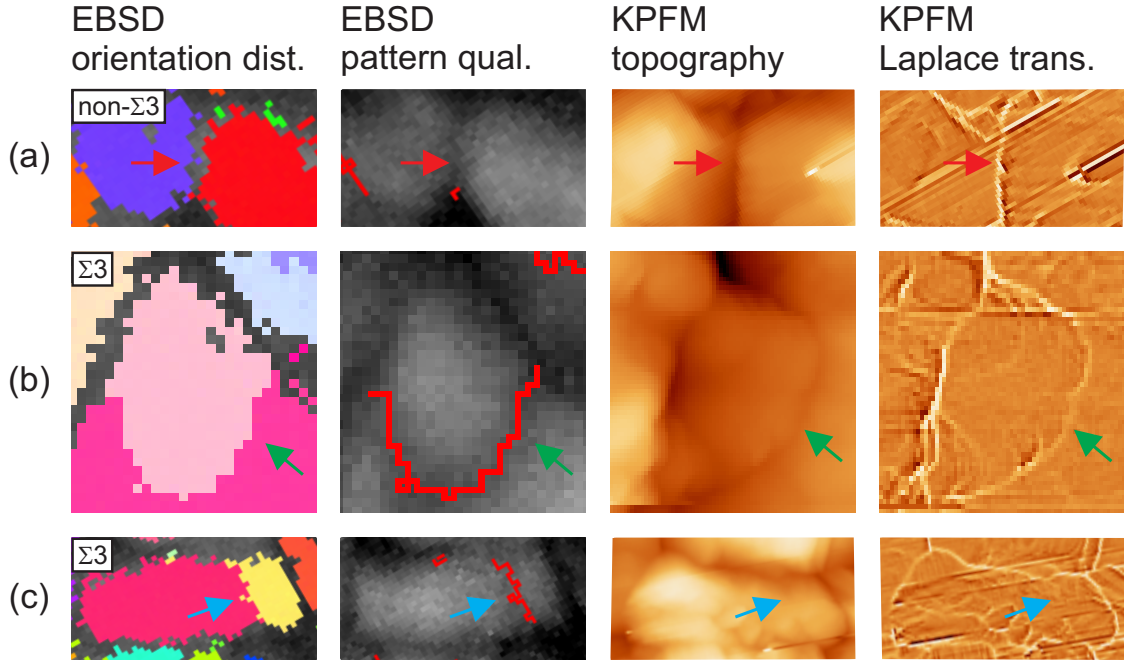From this analysis, we conclude that by a topography-based localization of GBs in CIGSe

FIG. 2. EBSD orientation-distribution and pattern-quality maps as well as KPFM images of topography and Laplace transformed $(\mathrm{d}^2 z/\mathrm{d}x^2 + \mathrm{d}^2 z/\mathrm{d}y^2)$ topography of (a) a non-$\Sigma 3$ GB with topography feature, (b) a $\Sigma 3$ GB with topography feature, and (c) a $\Sigma 3$ GB without topography feature. $\Sigma 3$ GBs are highlighted in the EBSD pattern quality map by solid red lines. The locations of the GBs are indicated in all images by colored arrows. The locations of the GBs can also be seen in Fig. 1a.

TABLE II. Quantity and symmetry ($\Sigma3$/non-$\Sigma3$) of all identified GBs from the area of the CIGSe-0 thin film shown in Fig. 1, as identified solely based on the KPFM topography and based on the EBSD orientation distribution map.

	KPFM topography	EBSD pattern quality
$\Sigma3$	3	35
non-$\Sigma3$	22	62

thin films, we reliably identify the location of GBs. However, only about 25% of all GBs are identified, with a preference to non-$\Sigma3$ GBs.

B. Electronic properties of grain boundaries in CIGSe

1. Potential variations at grain boundaries

Based on the conclusion given above, we evaluate the measurements of the GB local potential variations of the five samples from Tab. I. Examplarily, the work function image of the CIGSe-0 sample is shown in Fig. 1d. Fig. 3a shows the electronic potential barriers at the GBs, obtained from an analysis of all KPFM work function images. This result is repeated from Ref.[22] and presents the starting point of the evaluations in the following. Twenty individual GBs are evaluated for each sample. Examplarily, Fig. S1[36] shows some extracted line profiles of the work function. A similar variation of potential barrier height (ΔV_{GB}) at GBs, in the range from about -100 to +100 mV, is observed for all samples. More details about the results shown in Fig. 3a are provided in Ref.[22].

The potential barriers observed in Fig. 3a are assigned to be caused by the presence of charged defect states at GBs[17,19,37–40]. The excess concentration of charge at a GB changes the electronic band structure and causes a band bending towards the GBs. The characteristics of this band bending, i.e., the sign of the potential barrier, depend on the sign of the net charge which is trapped at the GB. Three cases can be distinguished.

(i) Positive charge trapped at a GB (depletion). If positive charge is trapped at a GB, free holes (CIGSe is a *p*-type semiconductor) are repelled from the near GB region. Ionized acceptors (negatively charged) are left, forming a hole-depleted space charge region (SCR) that compensates the positive charge at the GB. A downward band bending toward the GB,
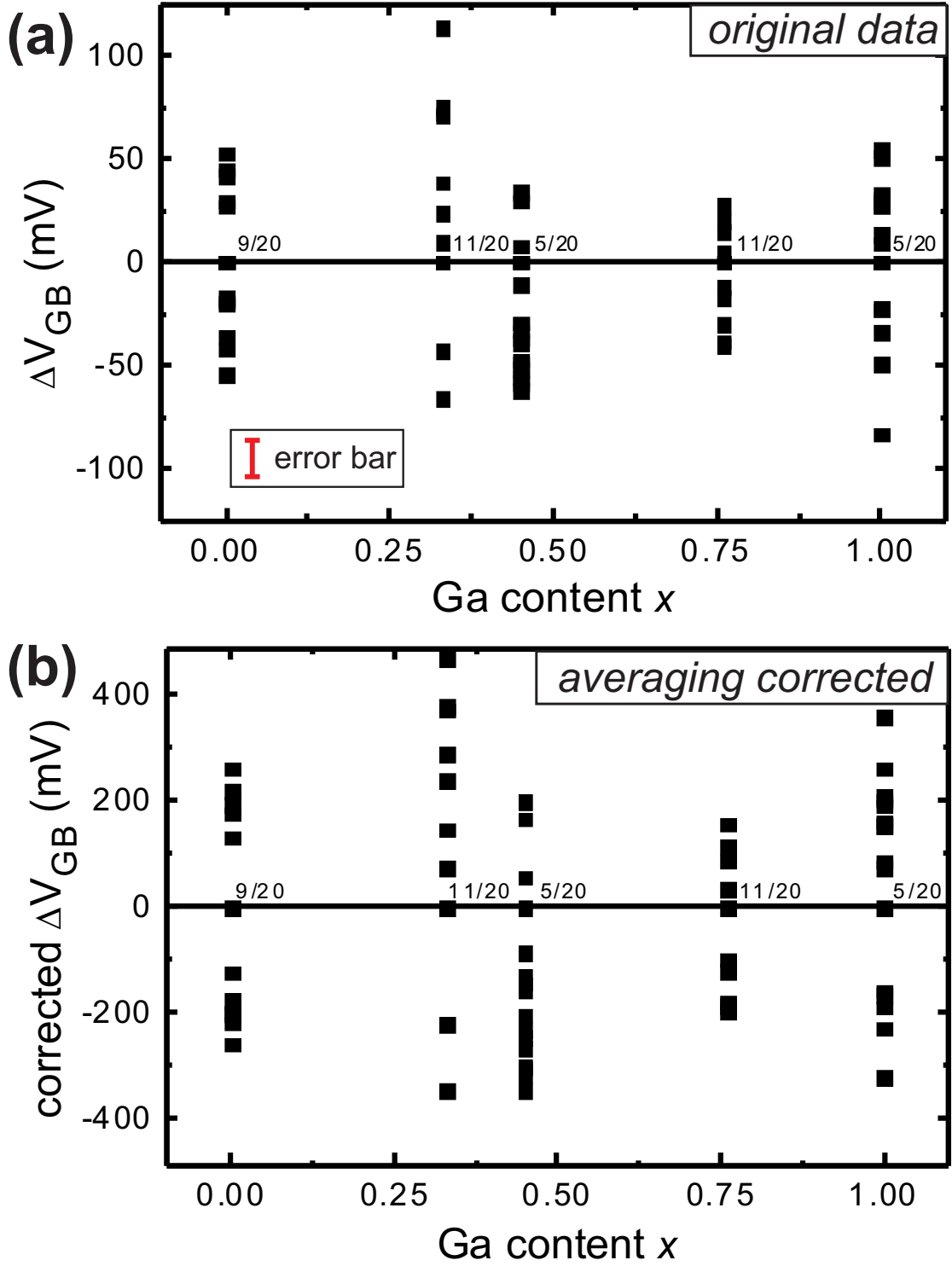
FIG. 3. Electronic potential barriers at GBs in dependence of the Ga content for the CIGSe thin films of Tab. I, (a) original data from the KPFM measurements, reproduced from Ref.[22], and (b) corrected data considering the averaging effect through the tip of the KPFM. A positive potential barrier represents an increase in local work function at the GB with respect to the grain surface, while a negative potential barrier indicates a decreased local work function at the GB. For each Ga content 20 GBs were evaluated. The number of GBs without a measurable potential barrier is indicated for each Ga content by the numbers.
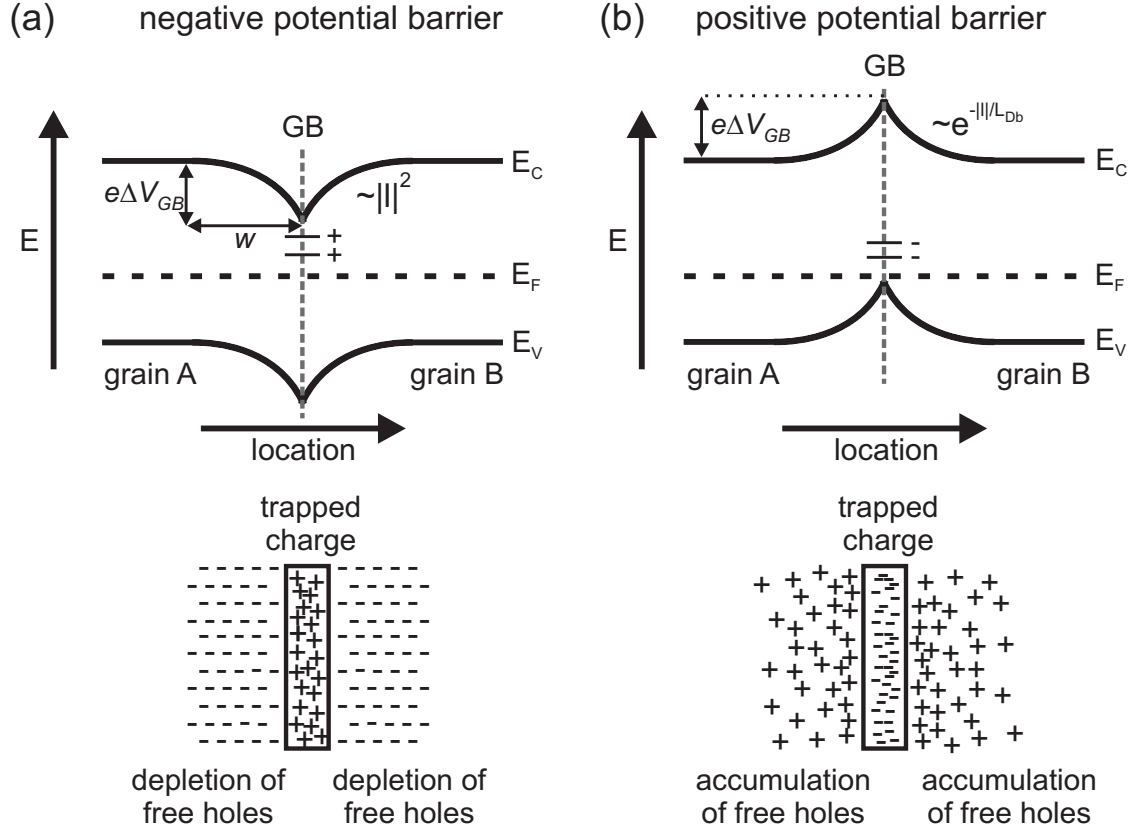
FIG. 4. Schematics of the electronic band diagram in the vicinity of GBs in CIGSe thin films for (a) a negative and (b) a positive potential barrier. Defect states (arbitrary) at the GB are indicated by a sequence of small dashes. Below the band diagrams 2-dimensional schematics of the specific charge compensation mechanisms in the case of a p-type semiconductor (i.e. CIGSe) are shown.

i.e. a negative potential barrier, is induced (Fig. 4a).

The potential distribution across a SCR can be calculated based on the Poisson equation and the Schottky approximation:

$$\epsilon\epsilon_0 \frac{\partial^2 V_{\mathrm{GB}}(l)}{\partial l^2} = -\rho(l) = -eP_{\mathrm{net}}, \tag{1}$$

where ϵ is the dielectric permeability of the CIGSe material, ϵ_0 is the dielectric constant, $V_{GB}(l)$ is the potential distribution across the GB, $\rho(l)$ is the charge density across the GB, l is the position, e is the elemental charge, and P_{net} is the net doping density of the p-type CIGSe material.

Two-time integration of Eq. (1) under consideration of suitable boundary conditions[41]

10

yields an expression for the potential distribution, i.e. the band bending, across the GB[42]:

$$V_{\mathrm{GB}}(l) = \frac{eP_{\mathrm{net}}}{2\epsilon\epsilon_0}(|l| - w)^2. \tag{2}$$

Here, $|l|$ is defined between 0 and w, where $l = 0$ is the location of the GB, and w is the width of the SCR which extends to both sides of the GB.

From this equation a relation between the potential barrier height ΔV_{GB} and the barrier width w of a GB can be derived:

$$\Delta V_{\mathrm{GB}} = \frac{eP_{\mathrm{net}}}{2\epsilon\epsilon_0}w^2. \tag{3}$$

For typical[38,51,52] charge carrier concentrations in the range of 10^{15} cm^{-3} to 10^{17} cm^{-3}, and potential variations in the range of 100 to 400mV the SCR width is on the order of 40 to 700nm. These values are well accessible in KPFM measurements.

(ii) Negative charge trapped at a GB (accumulation). If negative charge is trapped at a GB, free holes are accumulated in the near-GB region and compensate the trapped charge. An upward band bending towards the GB, i.e. a positive potential barrier, is induced (Fig. 4b). Considering only the majority carriers (holes) and with an approximation for small potential barriers, the potential distribution around the GB can be calculated from[44]:

$$tanh\left(\frac{eV_{\mathrm{GB}}(l)}{4k_{\mathrm{B}}T}\right) \cong tanh\left(\frac{eV_{\mathrm{GB}}(l = 0)}{4k_{\mathrm{B}}T}\right)exp\left\{-\sqrt{2}\frac{l}{L_{\mathrm{Db}}}\right\}, \tag{4}$$

where $L_{\mathrm{Db}} = \sqrt{\frac{\epsilon\epsilon_0 k_{\mathrm{B}}T}{e^2 P_{\mathrm{net}}}}$ is the Debye-length, and $l = 0$ is the location of the GB. Fig. 5 shows the calculated potential change to one side of the GB for two different ΔV_{GB} and two different P_{net}. The decay of the potential depends strongly on both, ΔV_{GB} and P_{net} and the decay lengths are somewhat smaller than the Debye lengths for the corresponding carrier concentrations. The length scale of the potential decay in Fig. 5 is in the range below the lower limit of the KPFM resolution, preventing an in-depth analysis of the potential barriers for negatively charged GBs. Furthermore, a simple analysis as in the case of positively charged GBs by a SCR width is not possible in this case. Extraction of values for the charge carrier concentration requires a fit to the potential peaks with two free parameters. Due to the noise level and the limitation in resolution a further analysis of the positive potential barriers is therefore not conducted. We note already here that experimentally the width of the GB potential change is similar for negatively and positively charged GBs; for the
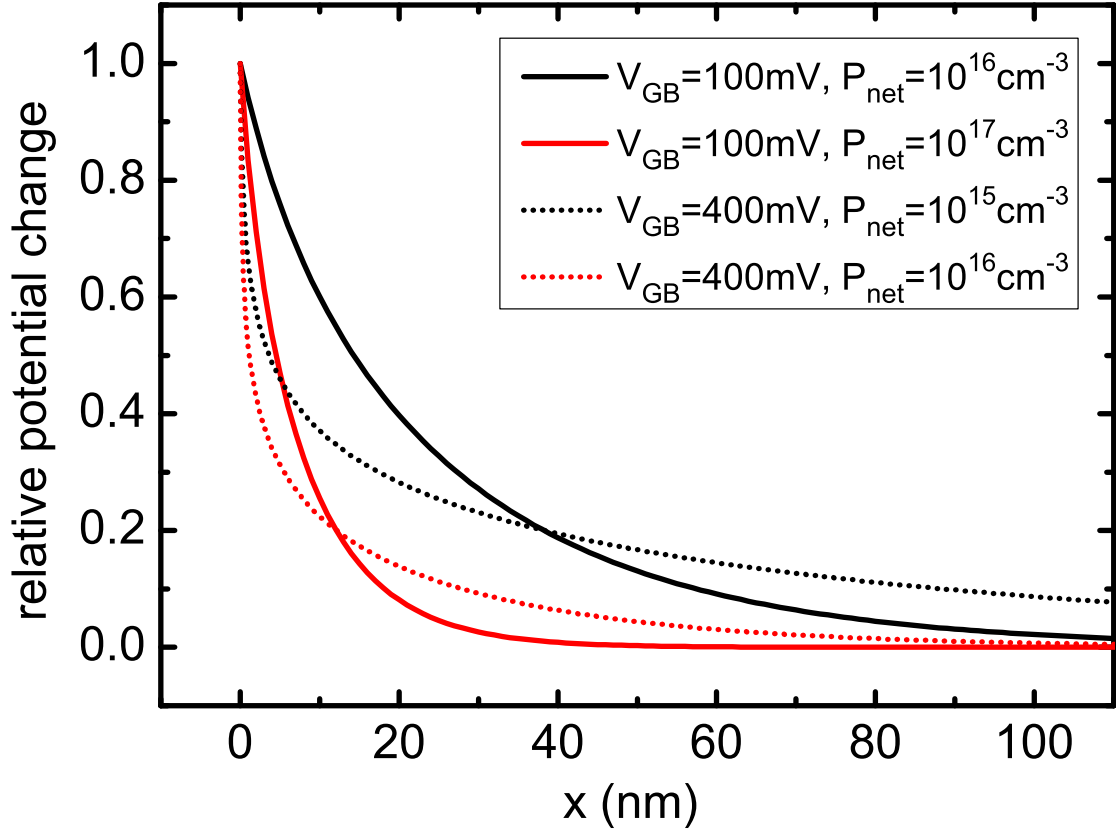
11

FIG. 5. Potential decay around a negatively charged GB for different potential peaks and charge carrier concentrations (see legend). The decay length is in the range of or below the spatial resolution of KPFM.

negatively charged GBs, the averaging effect in KPFM results in a widening of the potential profile, see Fig. S1[36] and the discussion in the next section.

(iii) No charges trapped at the GB. The GB is charge neutral[20]. Since there is no charges, no band bending results around the GB. This is the case for about 40% of all GBs, as indicated by the data points on the zero-line in Fig. 3a, where the numbers give the quantity of respective GBs with no potential variation.

2. *True potential barrier heights at grain boundaries*

Before a quantification of the GB potential barriers, doping concentrations, and defect densities can be made, the magnitude of the measured potential barrier heights has to be corrected by considering the averaging effect of KPFM measurements owing to the long-range nature of the involved electrostatic forces[26,27,30].

We have shown recently[30] that the magnitude of the averaging effect depends on the various geometry parameters of the experimental setup, namely the geometry of the used tip, the tip-sample distance, and the size of the detected potential variation[43]. All cantilevers used for the present study exhibit a similar tip-geometry[45], and the tip-sample distance is kept constant at $z \approx 10$ nm for all experiments. Consequently, the only geometry parameter affecting the magnitude of the averaging effect is the width (w) of the potential barriers.

Fig. 6a shows the widths of the potential variation of all electronically active GBs from Fig. 3a as a function of the Ga content. The widths were simply measured from line profiles across the grain boundaries, as previously described in Ref.[30]. A variation of the widths between ≈ 25 and 125 nm is determined, while no dependence on the Ga content is found. The variation in widths can be understood, considering the different potential-barrier heights observed in Fig. 3a. According to Eq. (2) and Eq. (4), different potential-barrier heights result in different barrier widths[46]. We would like to point out that the width of the positive potential barriers comprises their full extension.

The minimum barrier width of ≈ 25 nm found in the experiments can be explained considering the radius of the used tips ($r \approx 20$ nm); in general, the radius of the tip represents a lower limit for the spatial resolution of potential variations in KPFM[26–28]. Smaller potential variations can still be detected by KPFM; however, their widths appear widened in KPFM images. For this reason a detailed quantitative evaluation of the positive potential barriers, which are expected to be lower than the experimental resolution (see Fig. 5) is omitted.

In Fig. 6b, the measured values of the potential-barrier height of the electronically active GBs from Fig. 3a are plotted against their widths. Additionally, data gathered by means of FEM simulations are depicted (Fig. 6c). The simulation[47] data displays the fraction of a potential barrier, which is detected in KPFM experiments in dependence of the barrier width at a fixed tip-sample distance of $z = 10$ nm (detailed information about the FEM simulations are provided in Ref.[30]). By comparison of the experimental data with the simulation data the fraction of the full potential barrier detected experimentally by KPFM for every GB is determined. In order to incorporate this averaging effect in the analysis of the potential barriers, the simulation data is fitted with an analytic function[48]. Based on this fit function the magnitude of the averaging effect is calculated individually for each experimental potential barrier. The resulting real potential-barrier heights are plotted as a function of the Ga content for all five samples in Fig. 3b. No change in qualitative information is
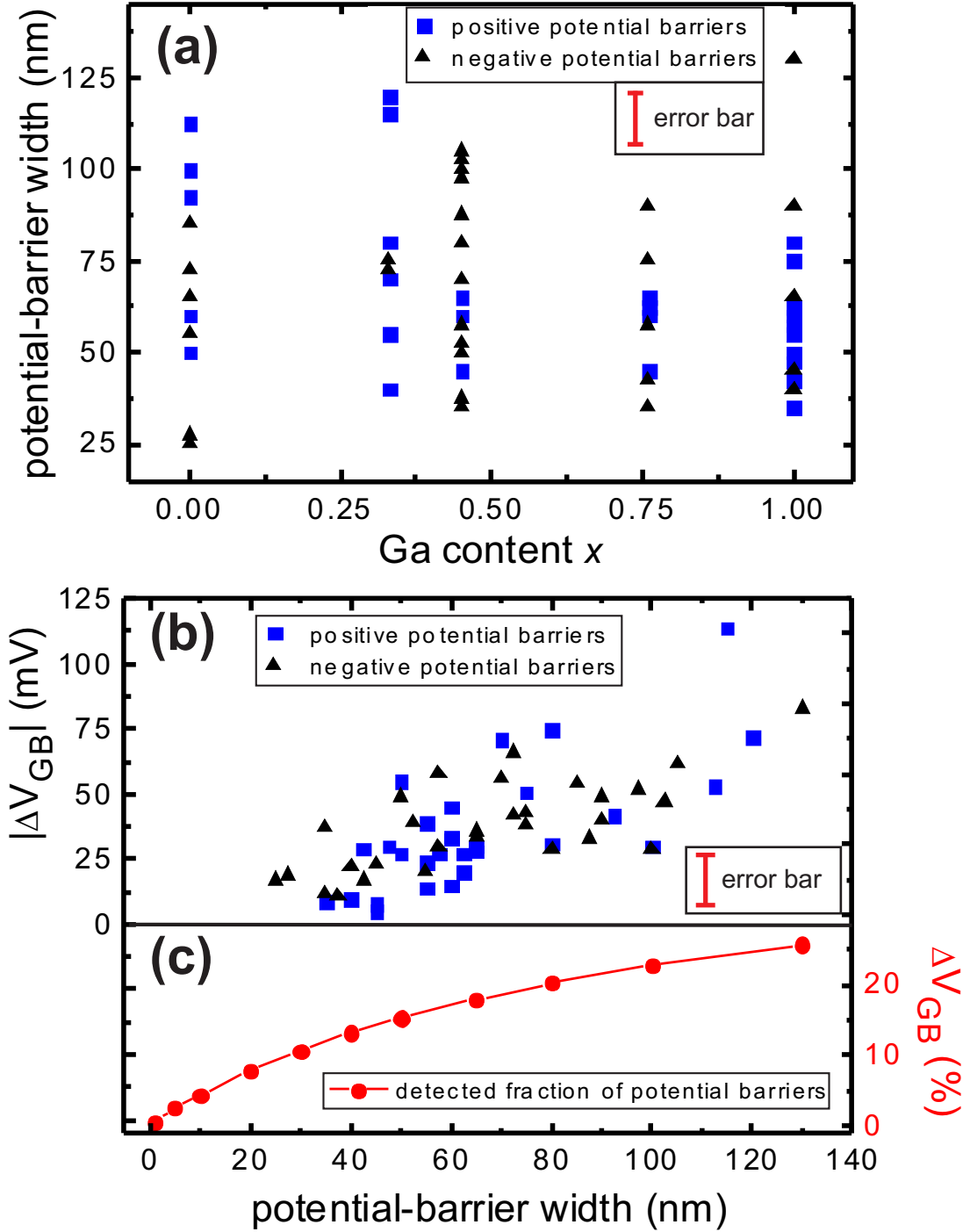
13

FIG. 6. (a) Potential-barrier widths of the electronically active GBs from Fig. 3a in dependence of the Ga content. (b) Measured potential-barrier heights of the electronically active GBs as a function of their width. (c) FEM simulation results representing the fraction of the potential barriers detected in the KPFM experiments in dependence of the width at a fixed tip-sample distance of $z = 10$ nm. Using this curve, the measured potential-barrier heights are converted into the corrected potential-barrier heights of Fig. 3b.

noticed when comparing Fig. 3a with b. The main difference between both figures is the magnitude of the potential barriers. Due to the incorporation of the averaging effect, it is increased by a factor between 4 and 10, depending on the width of the respective potential barrier.

3. *Doping densities and defect densities*

Using the corrected potential-barrier heights of Fig. 3b, we can now continue to analyze the GBs quantitatively and extract values for the doping and defect densities. As discussed above, this analysis will only be performed for positively charged GBs.

In Fig. 7a the corrected values of the negative potential-barrier heights of Fig. 3b are plotted as a function of the square of the corresponding barrier widths. According to Eq. (3), a linear dependence of the data is expected in the case of a constant doping density P_{net}. However, a linear dependence is not observed in Fig. 7a, which suggests a non-constant effective doping density within the studied CIGSe thin films, possibly due to variations of the defect density within the films.

Using Eq. (3) we estimate the doping density P_{net} of the CIGSe thin films[49] to between 1.5×10^{16} cm^{-3} and 3.6×10^{17} cm^{-3} (Fig. 7a). These numbers are in good agreement with doping densities of CIGSe thin films reported in the literature[38,51,52].

In Fig. 7b the doping densities in the vicinities of the GBs with negative potential barriers are plotted as a function of the Ga content. For this purpose, P_{net} is calculated individually for each GB via Eq. (3). With these values we calculate the charge per unit area (Q_{SCR}) localized at the SCRs at both sides of a GB[11]:

$$Q_{SCR} = -2eP_{net}w. \tag{5}$$

$|Q_{SCR}|$ must be equal to the charge per unit area Q_{GB}, which is localized at the GB. Considering the relation between Q_{GB} and the defect density P_{GB} at a GB, $Q_{GB} = eP_{GB}$, Eq. (3) can be written as:

$$P_{GB} = \sqrt{\frac{8\epsilon\epsilon_0 P_{net}\Delta V_{GB}}{e}}. \tag{6}$$

The defect density of each individual GB with negative potential barrier height is calculated via Eq. (6), and plotted in Fig. 8 in dependence of the Ga content. The defect densities
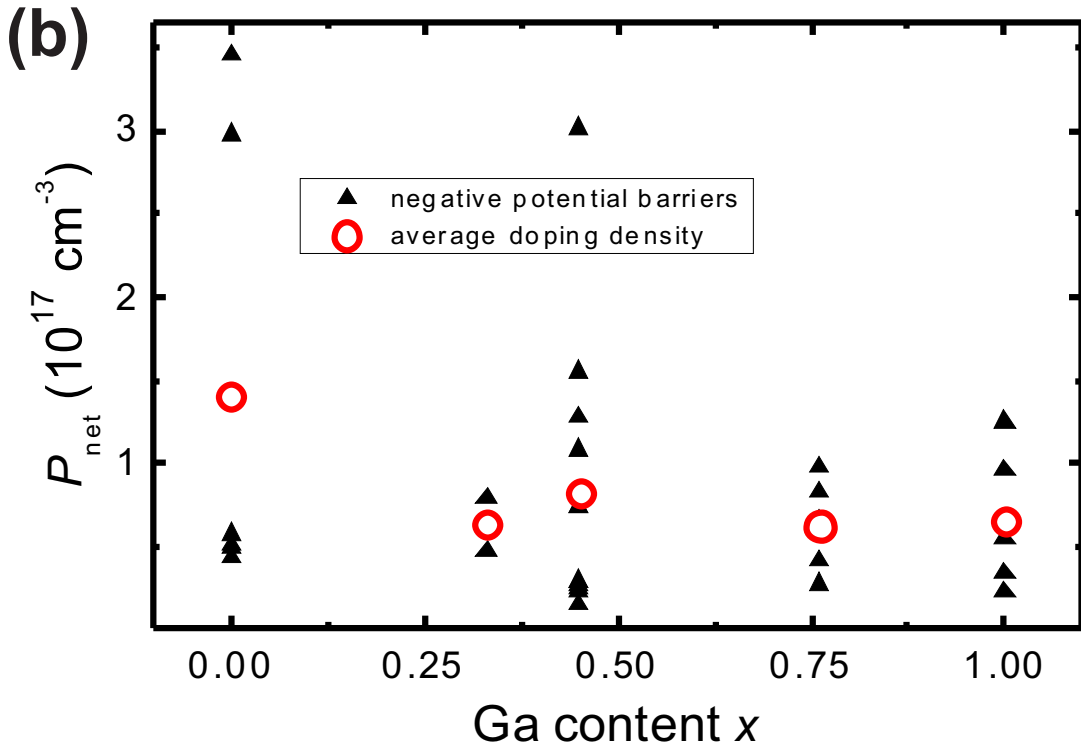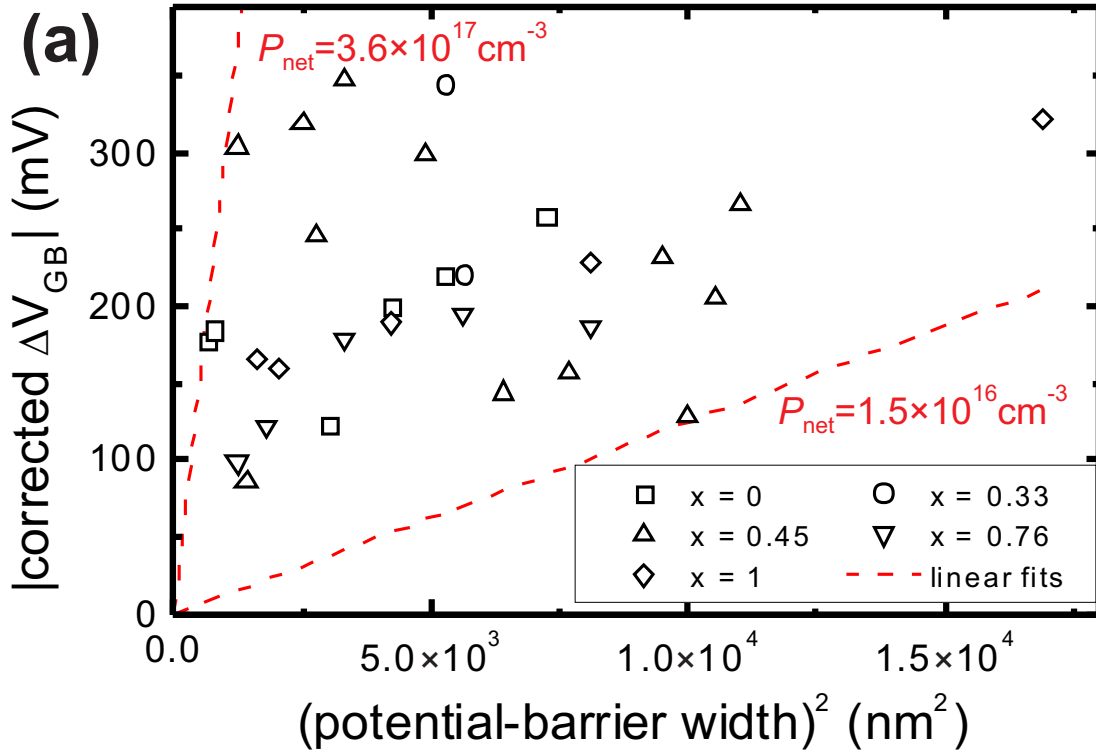
FIG. 7. (a) Corrected heights of negative potential barriers as a function of the square of the corresponding barrier widths. The linear fits indicate maximum and minimum doping densities P_{net} of the CIGSe thin films. (b) Doping densities P_{net} of CIGSe in the vicinities around the negative potential barriers in dependence of the Ga content.
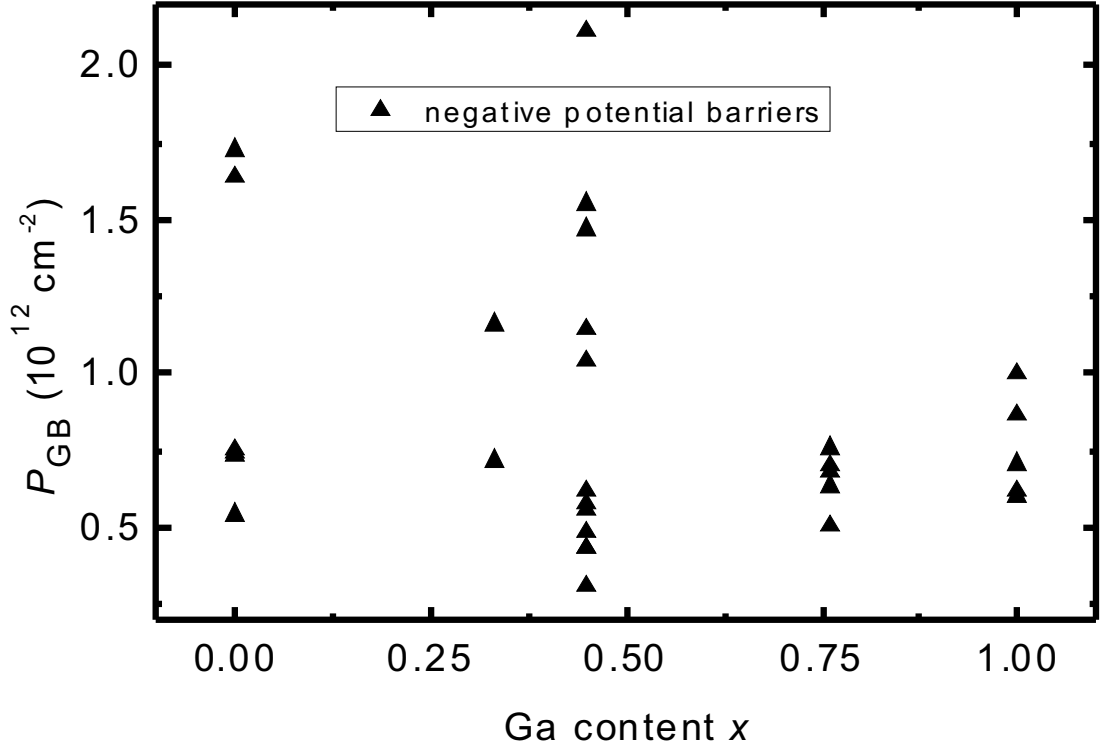
FIG. 8. Defect densities P_{GB} at GBs with negative potential barriers in dependence of the Ga content.

P_{GB} range between about 3.1×10^{11} cm^{-2} and 2.1×10^{12} cm^{-2}, which is in good agreement with defect densities at GBs of CIGSe thin films reported in the literature[19,38].

IV. DISCUSSION AND CONCLUSION

We have shown that for a topography-based localization of GBs no surface feature is wrongly misinterpreted as GB, if the strict criteria given in Sec. III A are applied. Lower symmetry non-$\Sigma 3$ GBs are preferentially selected over highly symmetric $\Sigma 3$ GBs by means of this localization method. Since $\Sigma 3$ GBs have a lower probability to exhibit charged potential barriers than non-$\Sigma 3$ GBs[33], an analysis of the electronic properties of GBs based on a GB localization using KPFM topography images thus overestimates the number of GBs with electronic potential barriers.

KPFM measurements of potential barriers at GBs in CIGSe thin films are subject to an averaging effect reducing the measured barrier height. The GB analysis presented in Sec. III B 1 provides a means to obtain the full height of the potential barriers by considering

17

the impact of the averaging effect[30]. This procedure allows a quantitative comparison of KPFM results to results obtained by other experimental techniques and to theory.

It is also shown that different charge compensation mechanisms are present in the cases of negative and positive charges localized at GBs of CIGSe thin films. While (in p-type semiconductors) positive charge at a GB is compensated by the formation of a space charge region, negative charge trapped at a GB leads to the accumulation of free holes in the vicinity of a GB. It is necessary to consider the different charge compensation mechanisms, to extract physical quantities from the experimental data, i.e. the charge carrier concentration of the CIGSe thin film and defect densities at GBs. The similar magnitude of the potential variation at positively and negatively charged GBs could indicate a similar energy level of the respnsible defect states. However, from our results we cannot determine the nature of the defect states.

Our analysis gives charge carrier concentrations between 1.5×10^{16} cm^{-3} and 3.6×10^{17} cm^{-3}. Variations in defect densities at GBs between 0.3 and 2.1×10^{12} cm^{-2} are determined. The presented results did not reveal any dependence of the electronic GB properties on the Ga content, contrary to claims of a relation between GB potential barriers and device efficiencies[17]; we note that in the latter work the samples were rinsed in de-ionized water to remove Na from the surface, where in our study we cannot exclude that Na diffuses to the surface during the UHV-anneal at 130°C. The variation of the charge carrier concentration by one order of magnitude, even within the same sample can be attributed to variations in the local composition. Qualitative lateral variations in the composition have been observed by microspot x-ray photoelectron spectroscopy[53]. Variations in the quasi Fermi level splitting observed by spatially resolved photoluminescence have also been attributed to variations in the composition[54,55]. The charge carrier concentration is mainly connected to the density of Cu vacancies, thus to the [Cu]/([In]+[Ga]) ratio. A systematic influence on the Ga content was not found in our study, which is to be expected as In and Ga are isoelectronic.

Finally, we would like to note that the methods and considerations presented here can be easily transfered to the analysis of GBs in other polycrystalline material systems.

V. ACKNOWLEDGMENT

REFERENCES

[1] T. I. Kamins, J. Appl. Phys. **42**, 4357 (1971).

[2] M. E. Cowher and T. O. Sedgwick, J. Electrochem. Soc. **119**, 1565 (1972).

[3] A. L. Fripp and L. H. Slack, J. Electrochem. Soc. **120**, 145 (1973).

[4] W. Siegel, G. Kühnel, and H. A. Schneider, phys. stat. sol. (a) **87**, 673 (1985).

[5] Y. Lo, J. Hong, M. Wu, and S. Wang, Electron Device Letters, IEEE **7**, 586 (1986).

[6] M. K. Sharma and D. P. Joshi, J. Appl. Phys. **102**, 033704 (2007).

[7] P. Jackson, D. Hariskos, E. Lotter, S. Paetel, R. Wuerz, R. Menner, W. Wischmann, and M. Powalla, Prog. Photovolt: Res. Appl. **19**, 894 (2011).

[8] C. Persson and A. Zunger, Phys. Rev. Lett. **91**, 266401 (2003).

[9] D. Fuertes Marrón, S. Sadewasser, A. Meeder, T. Glatzel, and M. C. Lux-Steiner, Phys. Rev. B **71**, 033306 (2005).

[10] Y. Yan, C. S. Jiang, R. Noufi, S.-H. Wei, H. R. Moutinho, and M. M. Al-Jassim, Phys. Rev. Lett. **99**, 235504 (2007).

[11] U. Rau, K. Taretto, and S. Siebentritt, Appl. Phys. A **96**, 221 (2009).

[12] M. Hafemeister, S. Siebentritt, J. Albert, M. C. Lux-Steiner, and S. Sadewasser, Phys. Rev. Lett. **104**, 196602 (2010).

[13] H. Mönig, Y. Smith, R. Caballero, C. A. Kaufmann, I. Lauermann, M. C. Lux-Steiner, and S. Sadewasser, Phys. Rev. Lett. **105**, 116802 (2010).

[14] R. Herberholz, V. Nadenau, U. Rühle, C. Köble, H. Schock, and B. Dimmler, Solar Energy Materials and Solar Cells **49**, 227 (1997).

[15] M. A. Contreras, L. M. Mansfield, B. Egaas, J. Li, M. Romero, R. Noufi, E. Rudiger-Voigt, and W. Mannstadt, Prog. Photovolt: Res. Appl. **20**, 843 (2012).

[16]W. Shockley and H. Queisser, J. Appl. Phys. **32**, 510 (1961).

[17]C.-S. Jiang, R. Noufi, K. Ramanathan, J. AbuShama, H. Moutinho, and M. Al-Jassim, Appl. Phys. Lett. **85**, 2625 (2004).

[18]C.-S. Jiang, M. A. Contreras, I. Repins, H. R. Moutinho, Y. Yan, M. J. Romero, L. M. Mansfield, R. Noufi, and M. M. Al-Jassim, Applied Physics Letters **101**, 033903 (2012).

[19]S. Sadewasser, T. Glatzel, S. Schuler, S. Nishiwaki, R. Kaigawa, and M. C. Lux-Steiner, Thin Solid Films **431-432**, 257 (2003).

[20]S. Siebentritt, S. Sadewasser, M. Wimmer, C. Leendertz, T. Eisenbarth, and M. C. Lux-Steiner, Phys. Rev. Lett. **97**, 146601 (2006).

[21]G. Hanna, T. Glatzel, S. Sadewasser, N. Ott, H. Strunk, U. Rau, and J. Werner, Applied Physics A: Materials Science & Processing **82**, 1 (2006).

[22]R. Baier, J. Lehmann, S. Lehmann, T. Rissom, C. A. Kaufmann, A. Schwarzmann, Y. Rosenwalks, M. C. Lux-Steiner, and S. Sadewasser, Sol. Energy Mater. Sol. Cells **103**, 86 (2012).

[23]Z. Zhang, X. Tang, O. Kiowski, M. Hetterich, U. Lemmer, M. Powalla, and H. Hölscher, Applied Physics Letters **100**, 203903 (2012).

[24]S. Sadewasser and T. Glatzel, *Kelvin Probe Force Microscopy - Measuring and compensating electrostatic forces* (Springer, Heidelberg, 2012).

[25]J. Colchero, A. Gil, and A. M. Baró, Phys. Rev. B **64**, 245403 (2001).

[26]T. Hochwitz, A. K. Henning, C. Levey, C. Daghlian, and J. Slinkman, J. Vac. Sci. Technol. B **14**, 457 (1996).

[27]U. Zerweck, C. Loppacher, T. Otto, S. Grafström, and L. Eng, Phys. Rev. B **71**, 125424 (2005).

[28]C. Leendertz, F. Streicher, M. C. Lux-Steiner, and S. Sadewasser, Appl. Phys. Lett. **89**, 113120 (2006).

[29]S. Sadewasser, C. Leendertz, F. Streicher, and M. C. Lux-Steiner, Nanotechnology **20**, 505503 (2009).

[30]R. Baier, C. Leendertz, M. C. Lux-Steiner, and S. Sadewasser, Phys. Rev. B **85**, 165436 (2012).

[31]H. Grimmer, W. Bollmann, and D. H. Warrington, Acta Crystallographica Section A **30**, 197 (1974).

[32]D. Abou-Ras, S. Schorr, and H. W. Schock, J. Appl. Crystallogr. **40**, 841 (2007).

[33]R. Baier, D. Abou-Ras, T. Rissom, M. C. Lux-Steiner, and S. Sadewasser, Appl. Phys. Lett. **99**, 172102 (2011).

[34]C. A. Kaufmann, R. Caballero, T. Unold, R. Hesse, R. Klenk, S. Schorr, M. Nichterwitz, and H. W. Schock, Solar Energy Mater. Solar Cells **93**, 859 (2009).

[35]C. Sommerhalter, T. Matthes, T. Glatzel, A. Jäger-Waldau, and M. C. Lux-Steiner, Appl. Phys. Lett. **75** (1999).

[36]Supplementary Information to this article. ....

[37]J. Seto, J. Appl. Phys. **46**, 5247 (1975).

[38]S. Schuler, S. Nishiwaki, J. Beckmann, N. Rega, S. Brehme, S. Siebentritt, and M. C. Lux-Steiner, in *Proceedings of the 29th IEEE conference* (IEEE,Piscataway, 2002) p. 504.

[39]M. J. Romero, K. Ramanathan, M. A. Contreras, M. M. Al-Jassim, R. Noufi, and P. Sheldon, Applied Physics Letters **83**, 4770 (2003).

[40]C.-S. Jiang, R. Noufi, J. AbuShama, K. Ramanathan, H. Moutinho, J. Pankow, and M. Al-Jassim, Appl. Phys. Lett. **84**, 3477 (2004).

[41]Electric field $\mathbf{E}(l = w) = 0$, potential barrier $V_{GB}(l = w) = 0$.

[42]L. Kronik and Y. Shapira, Surf. Sci. Rep. **37**, 1 (1999).

[43]Note that the assumption of quasi-neutrality, strictly speaking, does not hold for potential barriers observed at GBs in CIGSe. k_B is the Boltzmann constant, and T is the absolute temperature.

[44]V.-J. Lee and D.R. Mason, J. App. Phys. **34**, 2660 (1963).

[45]The GB topography has a negligible influence on the experimental results, as demonstrated in Ref.[30].

[46]Si cantilevers with Pt-Ir coated tip from the same manufacturer (EFM-PPP, *www.nanoworld.com*) were used for all experiments.

[47]Note that it is necessary to assume an experimental noise level in order to define the width of a potential barrier in the case of accumulation, as Eq. (4) only decays to 0 for $l \rightarrow \pm\infty$.

[48]For the simulation input parameters in accordance to the geometry of the experimental setup were used.

[49]$y = ax^{bx^{-c}}$, $a = 123.70486$, $b = 0.00232$, $c = 0.2367$.

[50]A dielectric permeability of $\epsilon = 11$ was used for all calculations within this section[56].

[51]L. Shay and J. Wernick, *Ternary Chalcopyrite Semiconductors* (Pergamon, Oxford, 1975).

[52]T. Eisenbarth, T. Unold, R. Caballero, C. A. Kaufmann, and H.-W. Schock, J. App. Phys. **107**, 034509 (2010).

[53]D. Eich, U. Herber, U. Groh, U. Stahl, C. Heske, M. Marsi, M. Kiskinova, W. Riedl, R. Fink, and E. Umbach, Thin Solid Films **361-362**, 258 (2000).

[54]L. Gütay, and G.H. Bauer, Thin Solid Films **487**, 8 (2005).

[55]L. Gütay, C. Lienau, and G.H. Bauer, App. Phys. Lett. **97**, 052110 (2010).

[56]N. Syrbu, M. Bogdanash, V. Tezlevan, and I. Mushcutariu, Physica B: Condensed Matter **229**, 199 (1997).